metals

MDPI

Article

Comparison of Charge Storage Properties of Prussian Blue Analogues Containing Cobalt and Copper

Amanda Rensmo and Jennifer R. Hampton *

Physics Department, Hope College, Holland, MI 49423, USA; rensmo.amanda@gmail.com
* Correspondence: hampton@hope.edu; Tel.: +1-616-395-7256

Received: 30 September 2019; Accepted: 10 December 2019; Published: 13 December 2019

Abstract: Prussian blue analogues are of great interest as alternative battery materials because of their long life cycle and potential use of earth-abundant elements. In this work, thin film mixed-metal hexacyanoferrates (HCFs) based on NiCo and NiCu alloys were fabricated in an all electrochemical process. The structure and composition of the samples were characterized, along with the charge storage capacity and kinetics of the charge transfer reaction. For both NiCo-HCF and NiCu-HCF samples, the total charge capacity increased with the substitution of Ni with more Co or Cu, and the increase was larger for Cu samples than for Co samples. On the other hand, the charge storage kinetics had only a modest change with substituted metal, and these effects were independent of the amount of that substitution. Thus, the mixed-metal HCFs have promise for increasing overall storage capacity without negatively influencing the rate capability when used in battery applications.

Keywords: Prussian blue analogues; alloys; electroformation; batteries; supercapacitors; energy storage

1. Introduction

Prussian blue analogues (PBAs) and other open framework intercalation compounds have been the subject of increasing interest as promising battery materials [1–6]. The general formula for PBAs can be written as $A_jM_k[M'(CN)_6]_l$, where M and M′ are transition metals, A is a counter cation, and the stoichiometry depends on the identities of M, M′, and A, as well as the number of cyanometalate vacancies incorporated into the structure [7]. Supercapacitive behavior occurs in these materials when the metal centers change oxidation state, accompanied by the intercalation or deintercalation of counter cations. For example, in the subset of PBAs known as hexacyanoferrates (HCFs), where M′ = Fe, one possible redox reaction is [7,8]

$$AM^{II}\left[Fe^{III}(CN)_6\right] + A^+ + e^- \leftrightarrow A_2M^{II}\left[Fe^{II}(CN)_6\right], \quad (1)$$

where in this example M is a divalent ion. The wide variety of transition metals that can be substituted for M and M′ makes tuning the properties of PBA materials a possibility. For example, by changing the transition metals, the potential of the redox reactions can be adjusted [9]. Thus, by appropriate choices of M and M′, PBAs can function as both the cathode and anode in a battery [10–12]. Mixed-metal PBAs have also been produced, where either M and M′ or both metals are occupied by a mixture of elements rather than just one, providing additional degrees of tunability [8,13–18].

In this work, mixed-metal HCFs were fabricated, where M was Ni, NiCo, or NiCu in various concentrations. In contrast to the nanoparticles that have been the focus of much of the PBA literature, the Ni-HCF electroformation method described by Borcarsly and coworkers [19–24] was adapted. Starting with electrodeposited NiCo and NiCu in various alloy compositions, NiCo-HCF and

NiCu-HCF were produced in an all electrochemical process through potential cycling in the presence of $K_3[Fe(CN)_6]$. The reactions leading to HCF formation can be written as

$$\left[Fe^{III}(CN)_6\right]^{3-}(aq) + M(s) + A^+(aq) \rightarrow \left[Fe^{III}(CN)_6\right]^{3-}(aq) + M^{2+}(aq) + A^+(aq) + 2e^- \rightarrow AM^{II}\left[Fe^{III}(CN)_6\right](s) + 2e^-, \quad (2)$$

where in this work, M = Ni, Co, Cu, or a mixture of metals. The thin film HCF was formed directly on the substrate surface, and the charge transfer properties of the materials were then measured without an additional electrode fabrication step. The goal was to investigate the effects of substituting Ni with Co or Cu for the case of electrogenerated thin film HCF. In particular, the charge storage capacity, redox reaction potential, and kinetic behavior of the charge storage reaction were measured as a function of the amount of substituted metal to the base Ni-HCF material.

2. Materials and Methods

All electrochemical fabrication and characterization steps were performed in a custom-built chemically inert Teflon cell with a working electrode area of 0.032 cm^2 [25] using a BASi Epsilon (Bioanalytical Systems, Inc., West Lafayette, IN, USA) or Gamry Interface 1000 (Gamry Instruments, Warminster, PA, USA) electrochemical workstation. A standard three-electrode set up was used with an Ag/AgCl (3M NaCl) reference electrode (Bioanalytical Systems), a Pt wire counter electrode and a gold wafer substrate working electrode. The substrate was prepared from a silicon wafer plated with 1000 Å of gold over a 50 Å titanium adhesion layer (Platypus Technologies, LCC, Madison, WI, USA). All electrolytes were prepared with salts from Sigma-Aldrich (St. Louis, MO, USA), used as received, and 18 MΩ·cm water purified using a Barnstead Nanopure Infinity (APS Water Services Corp., Van Nuys, CA, USA) or Milli-Q (MilliporeSigma, Burlington, MA, USA) system.

Films were deposited through controlled potential electrolysis by stepping the potential from open circuit to −1200 mV until 100 mC had been deposited. Deposition solutions contained 0.5 M H_3BO_3 and 1 M Na_2SO_4 with $NiSO_4$ and either $CuSO_4$ or $CoSO_4$ in various amounts. The total metal concentration was constant at 100 mM, of which $CuSO_4$ (below denoted as Cu samples) or $CoSO_4$ (below denoted as Co samples) consisted of 10, 15, 20 or 25%. The metal thin film was modified through cyclic voltammetry (CV) for 30 cycles from −200 to 1000 mV with a sweep rate of 50 mV/s in a solution containing 0.01 M $K_3[Fe(CN)_6]$ and 1 M Na_2SO_4 in order to form the HCF as shown in Equation (2). The charge storage capacity and kinetic behavior of the HCF was characterized in a blank solution of 1 M Na_2SO_4 with several CV scans with sweep rates from 10 to 1000 mV/s.

Structure and composition measurements, before and after the modification and characterization steps, were performed using a TM3000 Tabletop scanning electron microscope (SEM) (Hitachi, Tokyo, Japan) with a Quantax 70 energy dispersive X-ray spectroscopy (EDS) attachment (Bruker, Madison, WI, USA). SEM images were obtained at 2500× magnification and composition measurements were extracted from EDS spectra taken at 300× magnification to determine Ni, Cu, and Co relative compositions.

Several sets of samples were fabricated, with variations to the procedure above. For one set of samples, Set A, composition and structure were analyzed both before and after the modification step using SEM and EDS. Another set of samples, Set B, was fixed in the Teflon cell throughout the deposition, modification, and characterization steps. The latter set was investigated to avoid the uncertainty of replacing the sample in the custom-built Teflon cell, and thus no pre-modification composition and structure analysis was performed with SEM and EDS measurements. For this set, the range of measurements conducted in the characterization step was extended with sweep rates from 5 mV/s to 10,000 mV/s. Finally, for a small set, Set C, only Ni was used in the deposition step. These samples provided a reference for comparison of the mixed-metal samples in Sets A and B.

From the CV data, the total charge storage capacity was calculated by integrating the anodic current density, $j = \frac{i}{A}$, as a function of potential, E,

$$\frac{Q}{A} = \frac{1}{v}\int j(E)\, dE, \tag{3}$$

where v is the scan rate and A is the geometric area of the working electrode. In addition, the peak current density, j_p, and peak potential, E_p, for each anodic sweep were extracted.

Average results were calculated by grouping the samples by deposition solution percentage so that trends and variations between samples could be analyzed more clearly. Weighted averages,

$$\overline{x} = \frac{\sum_i w_i x_i}{w}, \tag{4}$$

and weighted standard deviations,

$$s = \sqrt{\frac{w\sum_i w_i (x_i - \overline{x})^2}{w^2 - \sum_i w_i^2}}, \tag{5}$$

were calculated from the individual measurements, x_i, and associated uncertainties, σ_i, where $w_i = \frac{1}{\sigma_i^2}$ are the weighting factors and $w = \sum_i w_i$ is the sum of the weights. Graphs of the individual results are included in the Supplementary Materials.

3. Results

To investigate the effect of the modification step on the metal composition, the relative amounts of the metals in the film were measured with EDS at a magnification of 300×. Figure 1 shows the composition of the samples in Set A before the modification step. The results show that the amount of Cu or Co in the film does not match the solution composition. This behavior is typical of metal deposition, particularly in the case of iron-group metals, where it is known as anomalous codeposition [26–30]. The Cu samples had large variations in composition whereas the Co samples had a clearer correlation between solution percentage of metal and deposited percentage of metal.

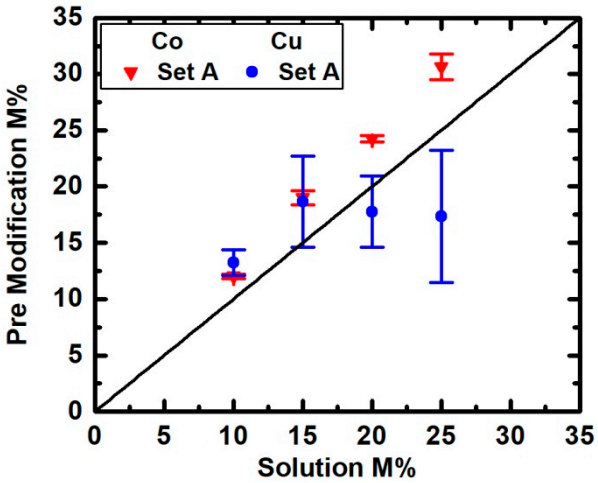

Figure 1. The dependence of the amount of deposited metal for each solution percentage for Set A. Results for the two alloys were grouped and averaged by deposition solution percentage. The line represents a 1:1 relationship. Figure S1 shows the results for the individual samples.

Figure 2 compares the composition results for the samples in Set A before and after the modification step. Some of the Cu samples lost up to half their amount of Cu, whereas no loss of Co was observed.

This is consistent with the observations that for NiCu alloys, Cu is selectively removed during electrochemical dealloying, whereas for NiCo alloys, neither metal is more stable compared to the other [31–34]. Thus, for the Cu samples here, the electrochemical modification step to form the HCF (CV cycles between −200 and 1000 mV) also removes some of the Cu.

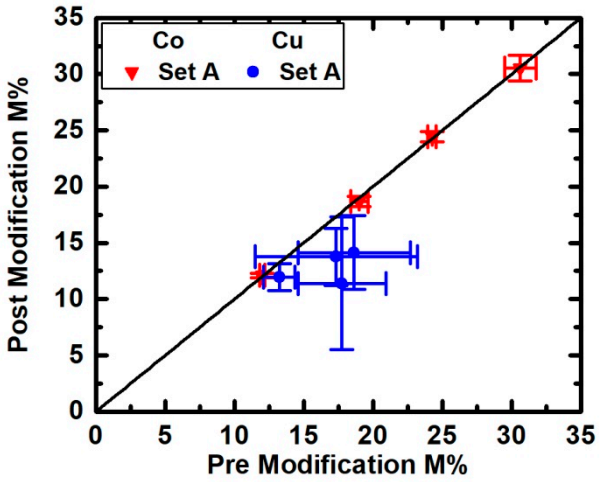

Figure 2. The dependence of the metal remaining after the modification step compared to the deposited metal for Set A. Results for the two alloys were grouped and averaged by deposition solution percentage. The line represents a 1:1 relationship. Figure S2 shows the results for the individual samples.

Figure 3 compares the solution percentage to post-modification composition for the samples in both Sets A and B. Similar trends were seen for both sets of samples with the Cu percentages being more scattered than those for Co. When comparing Set A and Set B, the nominally identical Cu samples were more consistent in the latter set when the electrochemical cell was not dismantled between the deposition and modification steps.

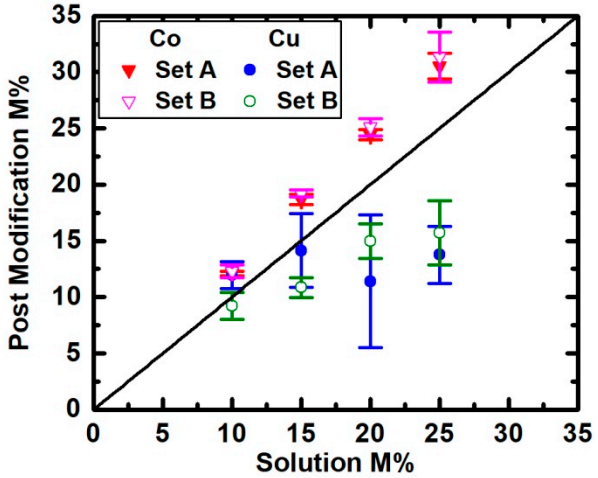

Figure 3. The dependence of the metal remaining after the modification step compared to the deposition solution percentage for Sets A and B. Results for the two alloys were grouped and averaged by deposition solution percentage. The line represents a 1:1 relationship. Figure S3 shows the results for the individual samples.

Figure 4 shows SEM images collected at 2500× magnification for a representative Co sample (a, b) and Cu sample (c, d) both before (a, c) and after (b, d) the modification step. In general, samples containing Co were smoother than those containing Cu. The Cu samples had a rough surface with dendrites, but no correlation was observed between the density of dendrites and the percentage of Cu.

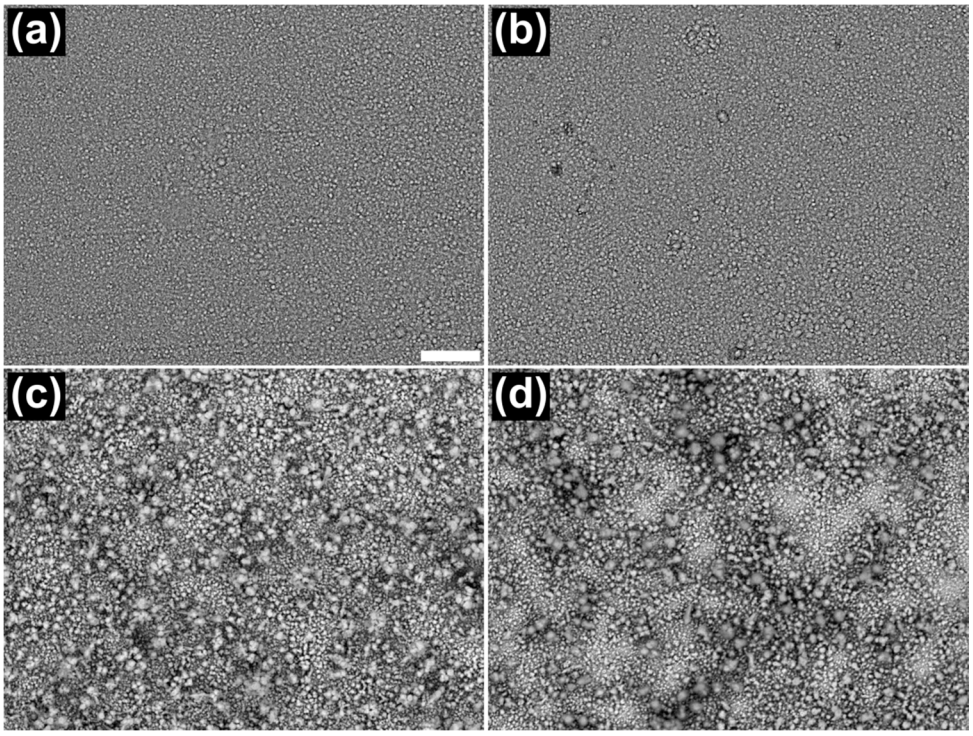

Figure 4. SEM images of a representative Co sample (**a**,**b**) and Cu sample (**c**,**d**) from Set A both before (**a**,**c**) and after (**b**,**d**) the modification step. The scale bar is 10 μm.

Representative CV scans are shown in Figure 5 for a Co sample (a) and a Cu sample (c). For both Co and Cu samples, either one oxidation and reduction peak or two closely-spaced, overlapping peaks were observed, corresponding to the redox reaction in Equation (1). The separation between the anodic and corresponding cathodic peaks increased with increasing scan rate, which is indicative of kinetic limitations and/or resistance effects for these samples.

The dependence of the anodic current density on sweep rate is shown in Figure 5b,d on a log-log scale. Insight into the kinetics of the reaction can be gained by performing a power-law fit, $j_p = av^b$, as shown in the figure. A value of b equal to 0.5 demonstrates a current dependent on semi-infinite linear diffusion, whereas a value of one illustrates a surface-controlled (capacitive) current [35]. In this case, an intermediate value of b was observed.

Additional kinetic analysis can be obtained by graphing the integrated charge per area as a function of scan rate, and fitting the data to the functional form described by Trasatti and coworkers,

$$\frac{Q}{A} = \frac{1}{A}\left(Q_{\text{cap}} + Q_{\text{diff}}\right) = \frac{1}{A}\left(k_1 + k_2 v^{-1/2}\right), \tag{6}$$

where Q_{cap} and Q_{diff} are the capacitive and diffusional contributions to the charge respectively [36,37]. From the fit parameters, k_1 and k_2, the two contributions can be quantified at specific scan rates. Representative examples of this analysis are shown in Figure S4, confirming that the charge storage kinetics for these samples is the result of mixed capacitive and diffusional behavior. Both an intermediate value of b in power-law fits and mixed kinetic behavior from Trasatti fits have been observed in a variety of intercalation charge storage systems [38–46].

The integrated charge capacity of the HCF films was calculated from 20 mV/s CV data. Because the total amount of HCF formed on the deposited metal is unknown, a charge per geometric area was calculated. Figure 6 shows that integrated charge per area vs. the amount of added metal to the film. The results showed that samples fabricated from NiCu alloys yield a significantly higher charge capacity than those from NiCo alloys. There is also a positive trend in charge capacity versus added

metal percentage for both types of samples. This effect is larger for the Cu samples, and therefore those samples can store more charge per substituted metal, compared to the Co samples.

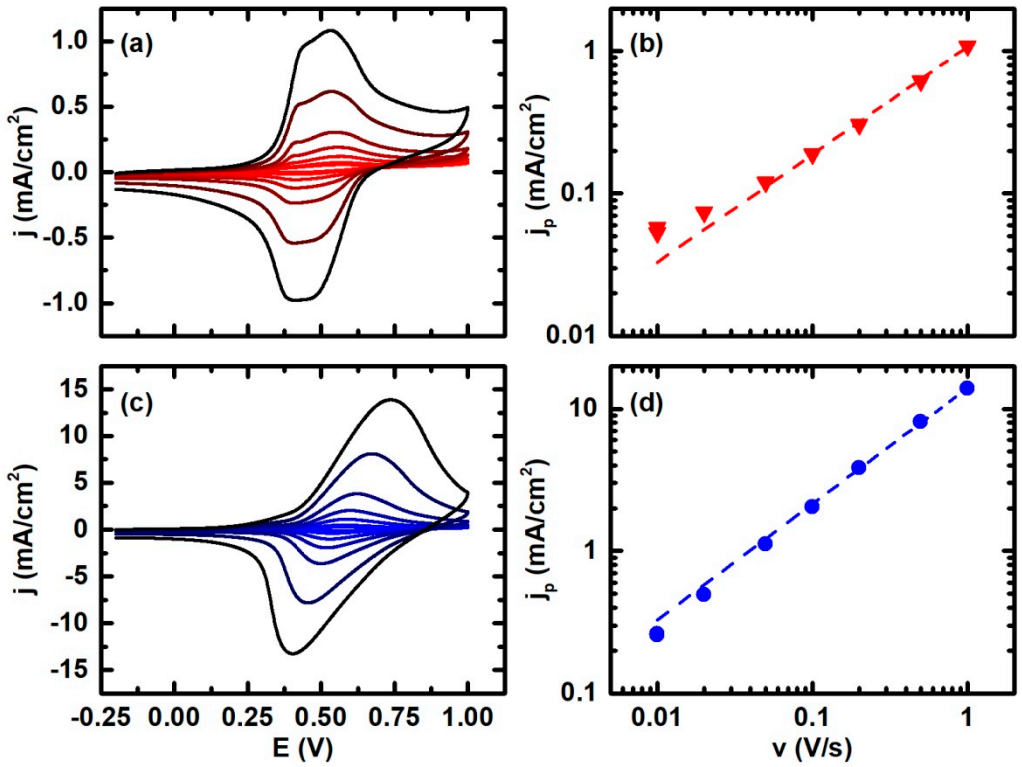

Figure 5. Example cyclic voltammetry (CV) scans from (**a**) a Co sample and (**c**) a Cu sample for scan rates from 10 mV/s to 1000 mV/s. The corresponding peak current density vs. v graphs are shown in (**b**) and (**d**) on a log-log scale with power law fits to $j_p = av^b$.

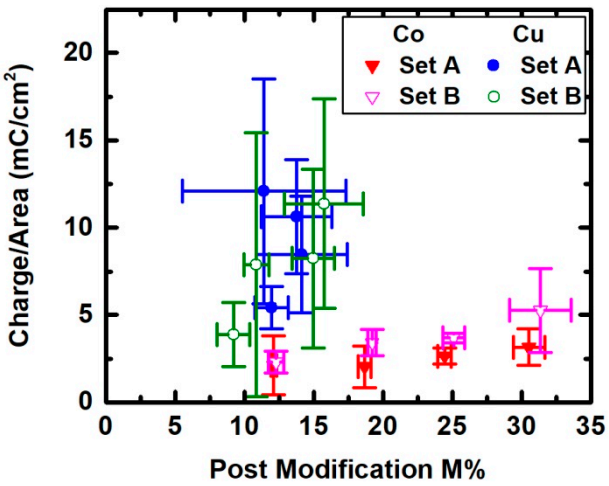

Figure 6. The measured anodic charge per area from the 20 mV/s CV as a function of the amount of added metal for Sets A and B. Results for the two alloys were grouped and averaged by deposition solution percentage. Figure S5 shows the results for the individual samples.

In Figure 7 the peak potentials for the samples extracted from the anodic sweep of a 20 mV/s CV scan are graphed vs. the amount of added metal. The peak potentials for the Cu samples are generally larger than for the Cu samples, but there is no correlation for either alloy between the percentage of added metal and the peak potential. The averages and standard deviations of the peak potentials were

calculated for each set as well as for the Co samples and Cu samples grouped together, and are listed in Table 1. The results for the single-metal Ni samples (Set C) are also listed. There is a fair amount of variability within and between sets; however, the average peak potential for the Cu samples is slightly higher than that for either the Co samples or solely Ni samples, which are statistically similar.

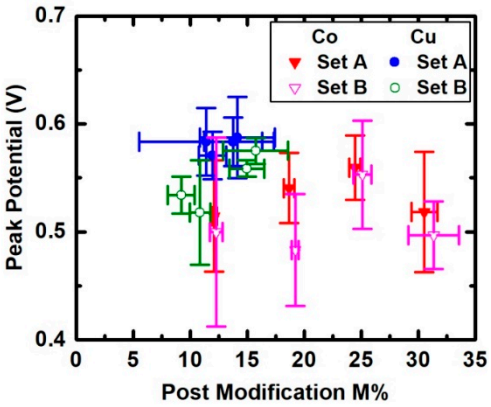

Figure 7. The anodic peak potential from the 20 mV/s CV as a function of the amount of added metal for Sets A and B. Results for the two alloys were grouped and averaged by deposition solution percentage. Figure S6 shows the results for the individual samples.

Table 1. Number of samples, N, weighted averages, and weighted standard deviations of the peak potentials, E_p, and power-law b-values for all the samples in each set and for the Co and Cu samples grouped together.

Set	N	$\overline{E_p}$ (V)	s_{E_p} (V)	$\bar{b}$	s_b
NiCo Set A	24	0.53	0.05	0.75	0.10
NiCo Set B	15	0.51	0.06	0.77	0.06
NiCo Sets A & B	39	0.52	0.05	0.76	0.09
NiCu Set A	24	0.58	0.03	0.84	0.03
NiCu Set B	14	0.55	0.03	0.83	0.04
NiCu Sets A & B	38	0.57	0.03	0.83	0.04
Ni Set C	4	0.537	0.024	0.713	0.012

The results of the kinetic analysis are shown in Figure 8. The b-values extracted from the power-law fits to anodic peak current density vs. scan rate are generally larger for the Cu samples than for the Co samples, and there is no observed trend between the metal concentration and the power-law exponent. The overall averages and standard deviations are listed in Table 1. Again, there is a good deal of variability between samples. The average b-value for the Cu samples is larger than that for the Co and Ni samples.

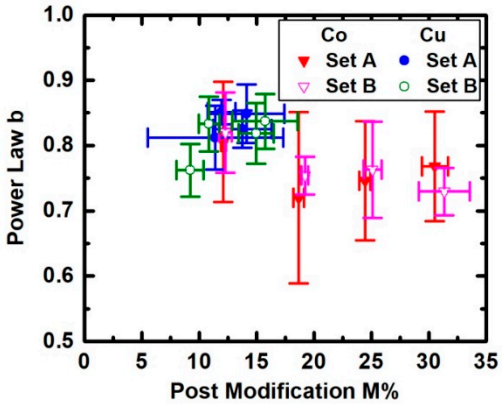

Figure 8. The *b*-value determined for a power-law fit to the anodic peak current density vs. scan rate as a function of the amount of added metal for Set A and B. Results for the two alloys were grouped and averaged by deposition solution percentage. Figure S7 shows the results for the individual samples.

4. Discussion

It was assumed that there would be increased reproducibility for the samples in Set B, when the electrochemical cell was not disassembled between the fabrication steps. For most of the quantities measured here, the standard deviations, measuring the ranges of results between nominally identical samples, were smaller for those in Set B compared to Set A. For example, the post modification percentage of Cu was not as scattered for Set B as for Set A (Figure 3). Furthermore, the uncertainties in the power-law fits were smaller and the precisions for the same measurements were better for both metals with this comparison (Figure 8). However, the opposite trend with the standard deviations is seen for the integrated charge for both metals, (Figure 6). Taken as a whole, the data between the sets are correlated, but Set B has better precision, which displays that reproducibility increased when all of the fabrication steps were performed without disassembling the electrochemical cell. As a result, while Set A was not prepared in the same way as Set B, it served as a structural reference for the more accurate measurements of Set B. Set B, in turn, was used to assess any differences in charge storage and kinetic behavior between the samples fabricated using different alloy percentages.

In comparison to the Co samples, the Cu samples showed a rougher surface in the SEM images and a greater loss of metals in the EDS data. These two outcomes can explain the difference in charge storage between the two types of added metals; a rougher surface results in a bigger surface area, and therefore the Cu samples react more during the modification step, yielding a larger charge per geometric area than for the Co samples. Both Co and Cu samples demonstrate that a higher substituted metal concentration yields a larger charge. However, the trend was not as clear for the Cu samples with more scattered data, which can be explained by the variances in remaining metal Cu after the modification step.

The power-law analysis showed that for the Cu samples, there was a modest increase in the kinetics of the charge storage reaction, closer to the ideal surface-bound response. For both the Co and Cu samples, the amount of added metal did not have a significant effect on the power-law results. Similar conclusions can be drawn for the peak potential; while there was a small increase in potential for the Cu samples, the potentials for all samples did not correlate with the extent of added metal. Taken together, these results show that substitution of either Cu or Co in Ni-HCF can increase the amount of charge that can be stored in the material without affecting the kinetics negatively.

5. Conclusions

In this work, mixed-metal PBA films were fabricated through an entirely electrochemical process, distinct from the nanoparticle fabrication methods which have been studied more often. The charge storage capacity and kinetics of the charge storage reaction were measured and compared with the structural and chemical outcomes. It was observed that the larger increase in charge per geometric area

of the Cu samples compared to the Co samples was correlated with a larger surface area. Furthermore, the substitution of Co or Cu in Ni-HCF changed the kinetics and the peak potential of the charge storage reaction a modest amount in some cases, and these changes were independent of the amount of added metal.

For these observations to be applied to practical charge storage devices, future work planned in our lab will include measurements quantifying the absolute amount of the metals in the starting alloy as well as the amount of PBA formed through the modification step, allowing for comparisons to PBA materials formed through other methods. Additionally, future work will take advantage of the all-electrochemical process for PBA fabrication highlighted here to explore the effects of underlying surface structure on the charge storage capacity of PBA films.

Supplementary Materials: The following are available online at http://www.mdpi.com/2075-4701/9/12/1343/s1, Figures S1–S3: Results for each individual sample corresponding to Figures 1–3 in the main text. Figure S4: Example Trasatti fits to integrated charge vs. scan rate. Figures S5–S7: Results for each individual sample corresponding to Figures 6–8 in the main text.

Author Contributions: conceptualization, A.R. and J.R.H.; funding acquisition, J.R.H.; investigation, A.R.; visualization, A.R. and J.R.H.; writing—original draft, A.R. and J.R.H.; writing—review and editing, J.R.H.

Funding: This research was funded by the U.S. National Science Foundation, RUI grant number DMR-1608327 and MRI grant number CHE-0959282.

Acknowledgments: We acknowledge support from Hope College Physics Department and the rest of the Surface Lab, including Scott Joffre.

Conflicts of Interest: The authors declare no conflict of interest.

References

1. Karyakin, A.A. Prussian Blue and Its Analogues: Electrochemistry and Analytical Applications. *Electroanalysis* **2001**, *13*, 813–819. [CrossRef]
2. De Tacconi, N.R.; Rajeshwar, K.; Lezna, R.O. Metal Hexacyanoferrates: Electrosynthesis, in Situ Characterization, and Applications. *Chem. Mater.* **2003**, *15*, 3046–3062. [CrossRef]
3. Huggins, R.A. Review—A New Class of High Rate, Long Cycle Life, Aqueous Electrolyte Battery Electrodes. *J. Electrochem. Soc.* **2017**, *164*, A5031–A5036. [CrossRef]
4. Ma, F.; Li, Q.; Wang, T.; Zhang, H.; Wu, G. Energy storage materials derived from Prussian blue analogues. *Sci. Bull.* **2017**, *62*, 358–368. [CrossRef]
5. Paolella, A.; Faure, C.; Timoshevskii, V.; Marras, S.; Bertoni, G.; Guerfi, A.; Vijh, A.; Armand, M.; Zaghib, K. A review on hexacyanoferrate-based materials for energy storage and smart windows: Challenges and perspectives. *J. Mater. Chem. A* **2017**, *5*, 18919–18932. [CrossRef]
6. Xing, Z.; Wang, S.; Yu, A.; Chen, Z. Aqueous intercalation-type electrode materials for grid-level energy storage: Beyond the limits of lithium and sodium. *Nano Energy* **2018**, *50*, 229–244. [CrossRef]
7. Li, C.H.; Nanba, Y.; Asakura, D.; Okubo, M.; Talham, D.R. Li-ion and Na-ion insertion into size-controlled nickel hexacyanoferrate nanoparticles. *RSC Adv.* **2014**, *4*, 24955–24961. [CrossRef]
8. Schwudke, D.; Stößer, R.; Scholz, F. Solid-state electrochemical, X-ray and spectroscopic characterization of substitutional solid solutions of iron–copper hexacyanoferrates. *Electrochem. Commun.* **2000**, *2*, 301–306. [CrossRef]
9. Scholz, F.; Dostal, A. The Formal Potentials of Solid Metal Hexacyanometalates. *Angew. Chem. Int. Ed.* **1996**, *34*, 2685–2687. [CrossRef]
10. Jayalakshmi, M.; Scholz, F. Charge–discharge characteristics of a solid-state Prussian blue secondary cell. *J. Power Sources* **2000**, *87*, 212–217. [CrossRef]
11. Jayalakshmi, M.; Scholz, F. Performance characteristics of zinc hexacyanoferrate/Prussian blue and copper hexacyanoferrate/Prussian blue solid state secondary cells. *J. Power Sources* **2000**, *91*, 217–223. [CrossRef]
12. Eftekhari, A. Fabrication of all-solid-state thin-film secondary cells using hexacyanometallate-based electrode materials. *J. Power Sources* **2004**, *132*, 291–295. [CrossRef]

13. Widmann, A.; Kahlert, H.; Petrovic-Prelevic, I.; Wulff, H.; Yakhmi, J.V.; Bagkar, N.; Scholz, F. Structure, Insertion Electrochemistry, and Magnetic Properties of a New Type of Substitutional Solid Solutions of Copper, Nickel, and Iron Hexacyanoferrates/Hexacyanocobaltates. *Inorg. Chem.* **2002**, *41*, 5706–5715. [CrossRef] [PubMed]
14. Widmann, A.; Kahlert, H.; Wulff, H.; Scholz, F. Electrochemical and mechanochemical formation of solid solutions of potassium copper(II)/zinc(II) hexacyanocobaltate(III)/hexacyanoferrate(III) $KCu_x\ Zn_{1-x}$ $[hcc]_x$ $[hcf]_{1-x}$. *J. Solid State Electrochem.* **2005**, *9*, 380–389. [CrossRef]
15. Wessells, C.D.; McDowell, M.T.; Peddada, S.V.; Pasta, M.; Huggins, R.A.; Cui, Y. Tunable Reaction Potentials in Open Framework Nanoparticle Battery Electrodes for Grid-Scale Energy Storage. *ACS Nano* **2012**, *6*, 1688–1694. [CrossRef]
16. Okubo, M.; Honma, I. Ternary metal Prussian blue analogue nanoparticles as cathode materials for Li-ion batteries. *Dalton Trans.* **2013**, *42*, 15881–15884. [CrossRef]
17. Yu, S.; Li, Y.; Lu, Y.; Xu, B.; Wang, Q.; Yan, M.; Jiang, Y. A promising cathode material of sodium iron–nickel hexacyanoferrate for sodium ion batteries. *J. Power Sources* **2015**, *275*, 45–49. [CrossRef]
18. Xie, M.; Xu, M.; Huang, Y.; Chen, R.; Zhang, X.; Li, L.; Wu, F. $Na_2Ni_xCo_{1-x}Fe(CN)_6$: A class of Prussian blue analogs with transition metal elements as cathode materials for sodium ion batteries. *Electrochem. Commun.* **2015**, *59*, 91–94. [CrossRef]
19. Bocarsly, A.B.; Sinha, S. Chemically-derivatized nickel surfaces: Synthesis of a new class of stable electrode interfaces. *J. Electroanal. Chem. Interfacial Electrochem.* **1982**, *137*, 157–162. [CrossRef]
20. Sinha, S.; Humphrey, B.D.; Bocarsly, A.B. Reaction of nickel electrode surfaces with anionic metal-cyanide complexes: Formation of precipitated surfaces. *Inorg. Chem.* **1984**, *23*, 203–212. [CrossRef]
21. Humphrey, B.D.; Sinha, S.; Bocarsly, A.B. Diffuse reflectance spectroelectrochemistry as a probe of the chemically derivatized electrode interface. The derivatized nickel electrode. *J. Phys. Chem.* **1984**, *88*, 736–743. [CrossRef]
22. Sinha, S.; Humphrey, B.D.; Fu, E.; Bocarsly, A.B. The coordination chemistry of chemically derivatized nickel surfaces generation of an electrochromic interface. *J. Electroanal. Chem. Interfacial Electrochem.* **1984**, *162*, 351–357. [CrossRef]
23. Amos, L.J.; Schmidt, M.H.; Sinha, S.; Bocarsly, A.B. Overlayer-support interactions associated with the formation of a chemically modified interface: The nickel ferrocyanide derivatized nickel electrode. *Langmuir* **1986**, *2*, 559–561. [CrossRef]
24. Amos, L.J.; Duggal, A.; Mirsky, E.J.; Ragonesi, P.; Bocarsly, A.B.; Fitzgerald-Bocarsly, P.A. Morphological variation at the $[NiFe(CN)_6]^{2-/-}$ derivatized nickel electrode: A technique for the evaluation of alkali cation containing solutions. *Anal. Chem.* **1988**, *60*, 245–249. [CrossRef] [PubMed]
25. Wozniak, N.R.; Frey, A.A.; Osterbur, L.W.; Boman, T.S.; Hampton, J.R. An electrochemical cell for the efficient turn around of wafer working electrodes. *Rev. Sci. Instrum.* **2010**, *81*, 034102. [CrossRef] [PubMed]
26. Akiyama, T.; Fukushima, H. Recent Study on the Mechanism of the Electrodeposition of Iron-Group Metal-Alloys. *ISIJ Int.* **1992**, *32*, 787–798. [CrossRef]
27. Grimmett, D.L.; Schwartz, M.; Nobe, K. A Comparison of DC and Pulsed Fe-Ni Alloy Deposits. *J. Electrochem. Soc.* **1993**, *140*, 973–978. [CrossRef]
28. Sasaki, K.Y.; Talbot, J.B. Electrodeposition of Iron-Group Metals and Binary Alloys from Sulfate Baths I. Experimental Study. *J. Electrochem. Soc.* **1998**, *145*, 981–990. [CrossRef]
29. Zech, N.; Podlaha, E.J.; Landolt, D. Anomalous codeposition of iron group metals I. Experimental results. *J. Electrochem. Soc.* **1999**, *146*, 2886–2891. [CrossRef]
30. Oriňáková, R.; Turoňová, A.; Kladeková, D.; Gálová, M.; Smith, R.M. Recent developments in the electrodeposition of nickel and some nickel-based alloys. *J. Appl. Electrochem.* **2006**, *36*, 957–972. [CrossRef]
31. Sun, L.; Chien, C.-L.; Searson, P.C. Fabrication of Nanoporous Nickel by Electrochemical Dealloying. *Chem. Mater.* **2004**, *16*, 3125–3129. [CrossRef]
32. Liu, Z.; Guo, L.; Chien, C.-L.; Searson, P.C. Formation of a Core/Shell Microstructure in Cu-Ni Thin Films. *J. Electrochem. Soc.* **2008**, *155*, D569–D574. [CrossRef]
33. Koboski, K.R.; Nelsen, E.F.; Hampton, J.R. Hydrogen evolution reaction measurements of dealloyed porous NiCu. *Nanoscale Res. Lett.* **2013**, *8*, 528. [CrossRef] [PubMed]
34. Peecher, B.E.; Hampton, J.R. Dealloying Behavior of NiCo and NiCoCu Thin Films. *Int. J. Electrochem.* **2016**, *2016*, 2935035. [CrossRef]

35. Bard, A.J.; Faulkner, L.R. *Electrochemical Methods: Fundamentals and Applications*, 2nd ed.; Wiley-Interscience: New York, NY, USA, 2001; ISBN 0-471-04372-9.
36. Ardizzone, S.; Fregonara, G.; Trasatti, S. "Inner" and "outer" active surface of RuO_2 electrodes. *Electrochim. Acta* **1990**, *35*, 263–267. [CrossRef]
37. Baronetto, D.; Krstajić, N.; Trasatti, S. Reply to "note on a method to interrelate inner and outer electrode areas" by H. Vogt. *Electrochim. Acta* **1994**, *39*, 2359–2362. [CrossRef]
38. Wang, J.; Polleux, J.; Lim, J.; Dunn, B. Pseudocapacitive Contributions to Electrochemical Energy Storage in TiO_2 (Anatase) Nanoparticles. *J. Phys. Chem. C* **2007**, *111*, 14925–14931. [CrossRef]
39. Yan, W.; Ayvazian, T.; Kim, J.; Liu, Y.; Donavan, K.C.; Xing, W.; Yang, Y.; Hemminger, J.C.; Penner, R.M. Mesoporous Manganese Oxide Nanowires for High-Capacity, High-Rate, Hybrid Electrical Energy Storage. *ACS Nano* **2011**, *5*, 8275–8287. [CrossRef]
40. Duay, J.; Sherrill, S.A.; Gui, Z.; Gillette, E.; Lee, S.B. Self-Limiting Electrodeposition of Hierarchical MnO_2 and $M(OH)_2/MnO_2$ Nanofibril/Nanowires: Mechanism and Supercapacitor Properties. *ACS Nano* **2013**, *7*, 1200–1214. [CrossRef]
41. Augustyn, V.; Come, J.; Lowe, M.A.; Kim, J.W.; Taberna, P.-L.; Tolbert, S.H.; Abruña, H.D.; Simon, P.; Dunn, B. High-rate electrochemical energy storage through Li^+ intercalation pseudocapacitance. *Nat. Mater.* **2013**, *12*, 518–522. [CrossRef]
42. Sankar, K.V.; Surendran, S.; Pandi, K.; Allin, A.M.; Nithya, V.D.; Lee, Y.S.; Selvan, R.K. Studies on the electrochemical intercalation/de-intercalation mechanism of $NiMn_2O_4$ for high stable pseudocapacitor electrodes. *RSC Adv.* **2015**, *5*, 27649–27656. [CrossRef]
43. Xia, C.; Guo, J.; Lei, Y.; Liang, H.; Zhao, C.; Alshareef, H.N. Rechargeable Aqueous Zinc-Ion Battery Based on Porous Framework Zinc Pyrovanadate Intercalation Cathode. *Adv. Mater.* **2018**, *30*, 1705580. [CrossRef] [PubMed]
44. Li, B.; Xi, B.; Feng, Z.; Lin, Y.; Liu, J.; Feng, J.; Qian, Y.; Xiong, S. Hierarchical Porous Nanosheets Constructed by Graphene-Coated, Interconnected TiO_2 Nanoparticles for Ultrafast Sodium Storage. *Adv. Mater.* **2018**, *30*, 1705788. [CrossRef] [PubMed]
45. Li, H.; Lang, J.; Lei, S.; Chen, J.; Wang, K.; Liu, L.; Zhang, T.; Liu, W.; Yan, X. A High-Performance Sodium-Ion Hybrid Capacitor Constructed by Metal–Organic Framework–Derived Anode and Cathode Materials. *Adv. Funct. Mater.* **2018**, *28*, 1800757. [CrossRef]
46. Dubal, D.; Jagadale, A.; Chodankar, N.R.; Kim, D.-H.; Gomez-Romero, P.; Holze, R. Polypyrrole Nanopipes as a Promising Cathode Material for Li-ion Batteries and Li-ion Capacitors: Two-in-One Approach. *Energy Technol.* **2019**, *7*, 193–200. [CrossRef]